

## Spatiotemporal structure of isodiffracting ultrashort electromagnetic pulses

Simin Feng\* and Herbert G. Winful†

*Department of Electrical Engineering and Computer Science, University of Michigan, 1301 Beal Avenue, Ann Arbor, Michigan 48109-2122*

(Received 15 December 1998)

We present a model of isodiffracting single-cycle and few-cycle ultrashort electromagnetic pulses. The model is based on exact solutions of the time-dependent paraxial wave equation with space-time coupling effects included. The spatiotemporal structure of these pulses is characterized by a scaling parameter which relates off-axis pulse shapes to the axial temporal waveforms. Depending on the spectrum a pulse may transform itself from a single-cycle pulse to a multicycle pulse along the radial coordinate. This model is also used to describe recirculating pulses in a curved mirror cavity resonator. The Gouy phase shift contributes an absolute phase that results in a pulse-to-pulse temporal instability.

PACS number(s): 42.25.Bs, 42.65.Re, 41.20.Jb, 42.60.Da

### I. INTRODUCTION

The propagation of ultrashort laser pulses and other ultrawideband electromagnetic pulses is a subject of great current interest. In the optical regime pulses as short as 5.4 fs and containing fewer than two cycles of the carrier wave (wavelength  $\sim 800$  nm) have been generated directly from a mode locked laser [1]. The interest in this wavelength regime has been in the generation of even shorter pulses, in the characterization of the pulse temporal profile, and in the measurement and control of the absolute phase of the pulse. At longer wavelengths (e.g., in the terahertz regime) where single-cycle pulsed beams are routinely generated [2], there is interest in optimizing the diffraction properties of these pulses so that their energy is highly localized around the propagation axis. One scheme proposed for improving the directivity and efficiency of pulsed beams is the ‘‘isodiffracting aperture,’’ which involves source shaping in space-time so that all the frequency components in the field have the same collimating distance [3]. Recently a number of authors have pointed out that these isodiffracting pulses are natural spatiotemporal modes of a curved mirror cavity resonator [4,5]. An understanding of the properties of isodiffracting pulsed beams is particularly relevant for studying the spatiotemporal profiles of mode-locked laser pulses.

A number of general characteristics of isodiffracting pulsed beams have been established by Heyman [6]. These include the fact that they are the most general eigenwavepacket solutions of the time-dependent paraxial wave equation. Their initial data is propagated along the hyperbolic ray paths of monochromatic Gaussian beams. Along these ray paths the pulse temporal profile undergoes a Hilbert transform as the pulse propagates from the near field to the far zone. These features were also noted by us in a study of exact ‘‘electromagnetic directed energy pulse train’’ (EDEPT) solutions of the full Maxwell equations [5,7]. Other features of the evolution of isodiffracting pulsed beams, such as a transformation from multiple cycle to single-cycle temporal profiles along a radial coordinate [8],

are characteristics that depend on the particular choice of pulse spectrum.

Our purpose in this paper is to provide detailed results for the spatiotemporal evolution of isodiffracting pulses whose amplitude spectra are of the form  $\omega^p \exp(-\omega\tau_0)$ . Such spectra are often observed in terahertz experiments and can also be tailored to describe femtosecond laser pulses. In addition, they lead to closed-form solutions for the isodiffracting pulse in terms of elementary functions. We find that pulses with such spectra obey a simple scaling law that permits easy calculation of such quantities as pulse width, peak frequency, bandwidth, and number of oscillation cycles at any point in space given those quantities at some other point. We also elucidate the role of the Gouy shift of finite beams in determining the absolute phase of an isodiffracting pulse. By absolute phase we refer to the phase of the carrier wave relative to the envelope. For recirculating pulses in a curved mirror cavity, we show that the Gouy shift causes the temporal profile of the transmitted pulses to vary from pulse to pulse in a quasiperiodic manner. These results are especially important for the generation and control of few-cycle mode locked laser pulses.

### II. MODELING OF ULTRASHORT PULSES

The pulsed Gaussian beams (PGB) are exact solutions of the time-domain paraxial wave equation [6],

$$\left\{ \nabla_{\perp}^2 - \frac{2}{c} \frac{\partial}{\partial t'} \frac{\partial}{\partial z} \right\} E(\mathbf{r}, t') = 0, \quad (2.1)$$

where  $\nabla_{\perp}^2$  operates on transverse coordinates, and  $t' = t - z/c$  is the local time. This equation can be obtained from an inverse Fourier transform of the frequency-domain paraxial wave equation

$$\left\{ \nabla_{\perp}^2 + 2ik \frac{\partial}{\partial z} \right\} \tilde{E}(\mathbf{r}, \omega) = 0 \quad (2.2)$$

with respect to the local time  $t' = t - z/c$ , where  $k = \omega/c$ . In the single-cycle regime the pulse longitudinal spatial extent  $c\tau_p$  (where  $\tau_p$  is the pulse width) is of order  $\lambda_p$  (the peak wavelength). Since the paraxial approximation holds when a

\*Electronic address: sfeng@umich.edu

†Electronic address: winful@eecs.umich.edu

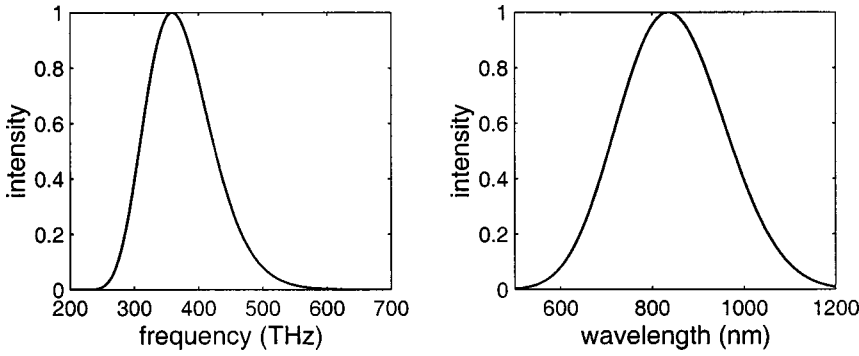


FIG. 1. Typical spectrum (in frequency and wavelength) used in the subsequent plots. The spectral range is referred to the typical spectrum of few-cycle mode-locked Ti:sapphire laser pulses. Here  $f_0 = 0.2 \text{ fs}^{-1}$  and  $\tau_0 = 5 \text{ fs}$ .

beam's Rayleigh length  $z_R$  is much greater than  $\lambda_p$ , for single-cycle pulsed beams we require  $c\tau_p \ll z_R$ . This condition can also be obtained by taking the inverse Fourier transform of the paraxial condition  $|\partial^2 \tilde{E}(\mathbf{r}, \omega) / \partial z^2| \ll |\omega/c \partial \tilde{E}(\mathbf{r}, \omega) / \partial z|$ , with respect to the local time  $t' = t - z/c$ , resulting in

$$\left| \frac{\partial^2 E(\mathbf{r}, t')}{\partial z^2} \right| \ll \left| \frac{1}{c} \frac{\partial^2 E(\mathbf{r}, t')}{\partial z \partial t'} \right|. \quad (2.3)$$

Since

$$\left| \frac{\partial E(\mathbf{r}, t')}{\partial t'} \right| \sim \left| \frac{E(\mathbf{r}, t')}{\tau_p} \right|$$

and

$$\left| \frac{\partial E(\mathbf{r}, t')}{\partial z} \right| \sim \left| \frac{E(\mathbf{r}, t')}{z_R} \right|,$$

Eq. (2.3) yields  $c\tau_p \ll z_R$  as the paraxial condition in the time domain. Moreover, in the paraxial regime the pulse looks like a ‘‘pancake,’’ i.e.,  $c\tau_p \ll 2w$  (where  $w$  is the transverse radius of the pulse), since the diffraction angle  $\lambda_p/2w \ll 1$ .

The fundamental Gaussian beam solution of the paraxial wave equation is given by [9]

$$\Psi(\mathbf{r}, \omega) = \frac{1}{z - iz_R} \exp\left(\frac{ik\rho^2}{2(z - iz_R)}\right), \quad (2.4)$$

where  $z_R$  is the Rayleigh range, and  $\rho^2 = x^2 + y^2$ . An isodiffracting pulsed Gaussian beam can be obtained by multiplying this solution by any square integrable spectrum  $\tilde{F}(\omega)$  and transforming back to the time domain. The resulting pulse is isodiffracting in the sense that all the frequency components have the same Rayleigh range. The Fourier components of the field are described by

$$\tilde{E}(\mathbf{r}, \omega) = \frac{\tilde{F}(\omega)}{z - iz_R} \exp\left(\frac{ik\rho^2}{2(z - iz_R)}\right), \quad \text{for } \omega > 0. \quad (2.5)$$

The details of the pulse spatiotemporal evolution will depend on the particular choice of spectrum  $\tilde{F}(\omega)$ . Here we choose spectra of the form  $\omega^p \exp(-\omega\tau_0)$  ( $\omega \geq 0$ ), where  $p (\geq 1)$  and  $\tau_0 (> 0)$  are real constants that can be determined from the peak frequency and bandwidth of the pulse. To model femtosecond laser pulses we include a low-frequency cutoff  $\omega_0$  below which the spectral amplitude is zero. In lasers the

low-frequency cutoff is determined by factors that include the bandwidth of the gain medium, cavity geometry, mirror bandwidth, and finite apertures. We thus take the spectrum as

$$\tilde{F}_p(\omega) = -i \frac{\pi A_0}{\Gamma(p+1)} (\omega - \omega_0)^p \times \exp[-(\omega - \omega_0)\tau_0] \theta(\omega - \omega_0), \quad (2.6)$$

where  $\theta(\omega - \omega_0)$  is a unit step function and  $A_0$  is a constant.  $\Gamma()$  is the gamma function. The step function ensures that there are no negative frequency components. This makes the time domain complex field an analytic function that is well behaved for all time and at all points in space. The low-frequency cutoff  $\omega_0$  is a positive parameter that can be identified as the carrier frequency of the pulse. The peak frequency of the pulse is given by  $\omega_p = \omega_0 + p/\tau_0$ , where the term  $p/\tau_0$  marks the location of the maximum of the unshifted spectrum  $\omega^p \exp(-\omega\tau_0)$ . The form of the coefficient in front of the above spectrum is chosen in order to simplify the final form of the time domain expressions. By varying  $\omega_0$ ,  $\tau_0$ , and  $p$ , Eq. (2.6) can be used to describe pulses that vary from a single cycle to an arbitrary number of cycles with any low-frequency cutoff. In this paper we use Eq. (2.6) to represent both terahertz and mode-locked laser pulses. Figure 1 shows a typical spectrum used in the subsequent plots in this paper. The wavelength range is referred to a typical spectrum for few-cycle mode-locked Ti:sapphire laser pulses.

The inverse Fourier transform of the electric field is defined by

$$E(\mathbf{r}, t) = \frac{1}{2\pi} \int_{-\infty}^{+\infty} \tilde{E}(\mathbf{r}, \omega) \exp(-i\omega t + ikz) d\omega, \quad (2.7)$$

where  $k = \omega/c$ . The analytic signal corresponding to  $E(\mathbf{r}, t)$  is obtained by a one-sided inverse Fourier transform

$$E^+(\mathbf{r}, t) = \frac{1}{\pi} \int_0^{+\infty} \tilde{E}(\mathbf{r}, \omega) \exp(-i\omega t + ikz) d\omega, \quad \text{Im } t < 0. \quad (2.8)$$

The real field is obtained from  $E(\mathbf{r}, t) = \text{Re}\{E^+(\mathbf{r}, t)\}$ . Substituting Eq. (2.6) into Eq. (2.5), and then into Eq. (2.8), one obtains a family of analytic functions,

$$E_p^+(\mathbf{r}, t) = \frac{A_p(T, \mathbf{r}) \exp[-i\phi(z)]}{\sqrt{z^2 + z_R^2}} \exp[-i\omega_0\tau - \rho^2/w^2(z)], \quad (2.9)$$

where the Gaussian beam size,  $w^2(z) = (2cz_R/\omega_0)\{1 + (z/z_R)^2\}$ , is evaluated at the carrier frequency  $\omega_0$ . The Gouy phase shift is  $\phi(z) = \tan^{-1}(z/z_R)$ . The complex function  $A_p(T, \mathbf{r})$  is given by

$$A_p(T, \mathbf{r}) = \frac{A_0 \exp[-i\alpha_p(T)]}{(1+T^2)^{(p+1)/2} \eta^{p+1}(\mathbf{r}) \tau^{p+1}},$$

$$\alpha_p(T) = (p+1) \tan^{-1}(T), \quad (2.10)$$

where  $T$  is a dimensionless scaled local time (SLT). Its general form is

$$T(\mathbf{r}, t) \equiv \frac{\tau(\mathbf{r}, t)}{\tau_0 \eta(\mathbf{r})} = \frac{t - \frac{1}{c} \left\{ z + \frac{\rho^2}{2R(z)} \right\}}{\tau_0 \left\{ 1 + \frac{\rho^2}{a^2(z)} \right\}}, \quad (2.11)$$

where  $\tau(\mathbf{r}, t)$  is a radially dependent local time, defined by

$$\tau(\mathbf{r}, t) \equiv t - \frac{1}{c} \left\{ z + \frac{\rho^2}{2R(z)} \right\}. \quad (2.12)$$

Here  $R(z) = z\{1 + (z_R/z)^2\}$  is the radius of curvature of the wavefront. It will be seen that  $\tau_0$  yields the on-axis pulse width that is invariant upon propagation.  $\eta(\mathbf{r})$  is a spatially dependent scaling parameter that scales the off-axis pulse width, bandwidth, peak, and instantaneous frequencies. It is given by

$$\eta(\mathbf{r}) = \left\{ 1 + \frac{\rho^2}{a^2(z)} \right\}, \quad (2.13)$$

where

$$a^2(z) = 2c\tau_0 z_R \left\{ 1 + \left( \frac{z}{z_R} \right)^2 \right\} = \frac{p\lambda_p^o z_R}{\pi} \left\{ 1 + \left( \frac{z}{z_R} \right)^2 \right\}, \quad (2.14)$$

with  $\lambda_p^o = 2\pi c\tau_0/p$  as the on-axis peak wavelength of the unshifted envelope spectrum (with  $\omega_0 = 0$ ). The quantity  $a(z)$  represents the radial extent of the pulse envelope. From Eqs. (2.10) and (2.13), we see that when  $\rho = a$  the magnitude of the envelope decreases by a factor  $2^{p+1}$  compared to the value on axis  $\rho = 0$ . Substituting Eq. (2.12) into Eq. (2.9), it is clear that Eq. (2.9) is consistent with the conventional envelope-carrier pulse expression, i.e.,  $E(\mathbf{r}, t) = A(\mathbf{r}, t) \exp(-i\omega_0 t + ik_0 z)$  in which an infinite plane wave carrier is modulated by an envelope function. The carrier wave in Eq. (2.9), however, is not a plane wave, but a finite beam with curved phase fronts. For example, the curvature of the carrier wave is expressed in the radially dependent local time  $\tau$ . This effect is not included in the traditional envelope-carrier expression. Equation (2.9) describes highly localized space-time wavepackets that propagate in free space and maintain their wavepacket structure during propagation. They represent a set of focused propagating modes in free space. They are a class of eigen-wavepacket solutions of the time-domain paraxial wave equation with the family of spectra Eq. (2.6). These eigen-wavepackets evolve continuously from single-cycle pulses to multicycle pulses as the

carrier frequency  $\omega_0$  is varied from zero to values greater than the pulse bandwidth ( $\omega_0 > 1/\tau_0$ ).

Since the imaginary part of Eq. (2.9) is simply related to the real part by a  $\pi/2$  phase shift, both real and imaginary parts of Eq. (2.9) describe a family of PGBs with an arbitrary number of cycles. When  $\omega_0 = 0$ , Eq. (2.9) reduces to

$$E_p^+(\mathbf{r}, t) = \frac{A_p(T, \mathbf{r}) \exp[-i\phi(z)]}{\sqrt{z^2 + z_R^2}}. \quad (2.15)$$

The real and the imaginary parts of Eq. (2.15) represent a family of single-cycle pulses. This form of single-cycle pulse for the case  $p=2$  was obtained in previous papers by taking a paraxial approximation of the exact solution of the full wave Maxwell's equations. [5,10] The low-frequency cutoff is zero in the single-cycle pulse. The spatiotemporal evolution of single-cycle pulses is purely determined by the complex envelope function Eq. (2.15). Comparing Eqs. (2.9) and (2.15), a multicycle isodiffracting pulse is composed of a focused complex envelope and a focused carrier wave with Gaussian transverse distribution. Figure 2 shows the spatiotemporal evolution of a multicycle pulse with low-frequency cutoff  $f_0 = 0.3 \text{ fs}^{-1}$ . The Rayleigh range  $z_R = 50 \text{ mm}$ , and  $p=5$  for all the figures in this paper. A thorough discussion of the physical properties of this family of eigen-wavepackets for the case  $p=2$  and  $\omega_0=0$  was given in Ref. [5]. Here we generalize the results to multicycle pulses and point out the spatial temporal structure of these eigen-wavepackets.

### A. Scaling structure

Due to the complexity of the space-time coupling, the pulse width, frequency, and number of cycles of the ultrashort pulses vary from point to point in space, as shown in Fig. 3. In this section we will show that the spatiotemporal structure of these pulses is characterized by the scaling parameter  $\eta(\mathbf{r})$ , which is related to the spatial variations of the temporal and frequency information of ultrashort pulses. Note that the scaling parameter  $\eta(\mathbf{r}) = \text{const}$  is a set of hyperbolic ray trajectories of a Gaussian beam. On axis  $\eta(\mathbf{r}) = 1$ , and its value increases towards the pulse periphery. By using the radially dependent scaled local time that contains most of the essential features of isodiffracting pulses, the temporal and frequency quantities of these pulses can be easily predicted at any point in space.

The pulse width can be determined from the amplitude function  $A_p(T, \mathbf{r})$ . As expected, from Eq. (2.10) it is independent of the carrier frequency. It is only determined by the envelope spectrum. Using the half-width at  $1/e$  of the maximum, we find that the pulse width at any point in space is related to that on axis by the scaling parameter through

$$\tau_p(\mathbf{r}) = \tau_p^o \eta(\mathbf{r}), \quad (2.16)$$

where

$$\tau_p^o = \tau_0 \sqrt{8/p} = \frac{\sqrt{2p}}{\pi} \frac{\lambda_p^o}{c} \quad (2.17)$$

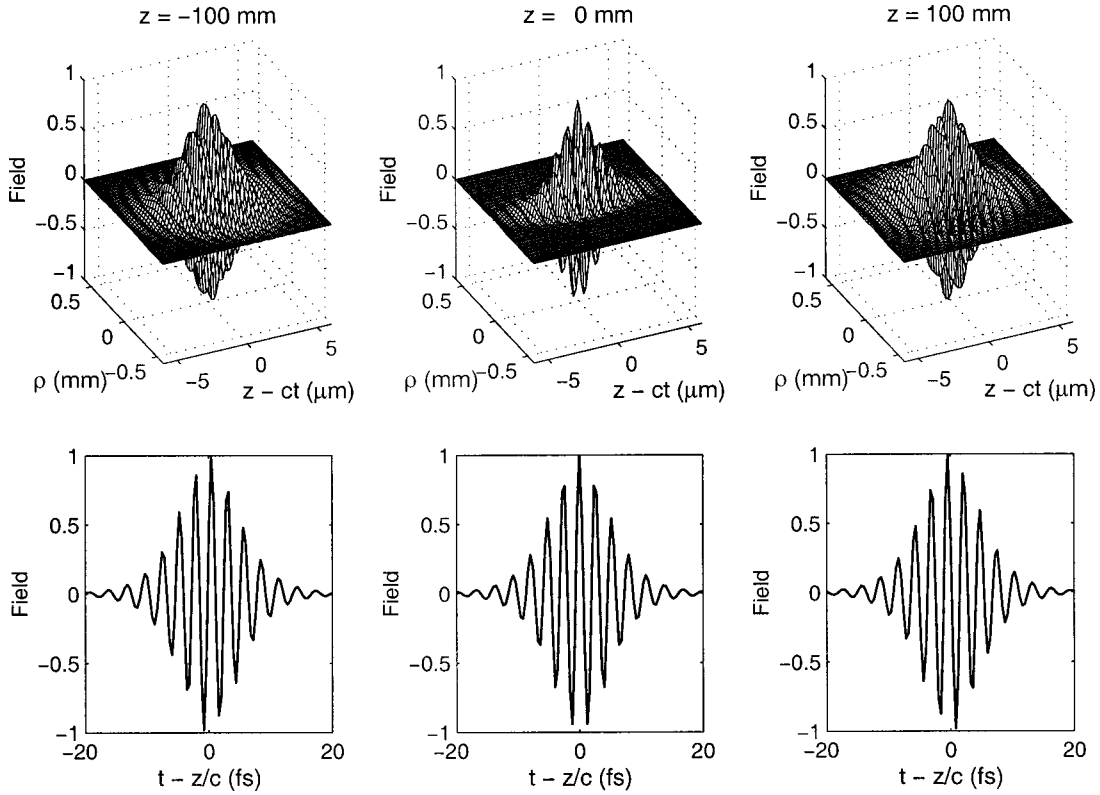


FIG. 2. Spatiotemporal evolution of a multicycle pulse with a low-frequency cutoff  $f_0 = 0.3 \text{ fs}^{-1}$  and  $\tau_0 = 11 \text{ fs}$ . The pulse propagates from the plane  $z = -100 \text{ mm}$  before the focus, through the focus, then to the plane  $z = 100 \text{ mm}$ . The plots in the top row are 3D plots, while the bottom row are on-axis ( $\rho = 0$ ) temporal profiles corresponding to the top row. The other parameters  $p = 5$ , and the Rayleigh range  $z_R = 50 \text{ mm}$  for this and subsequent plots.

is the pulse width on axis ( $\rho = 0, z$ ). In obtaining the expression for  $\tau_p^o$ , the approximation  $\exp[2/(p+1)] - 1 \approx 2/p$  was used (when  $p = 1$  the error is 14%, when  $p = 2$  the error is only 5%). The pulse width on axis is independent of the propagation distance  $z$  as the result of the isodiffracting nature of the pulse. The parameter  $\tau_0$  characterizes the pulse width on axis. The off-axis pulse width is increased by a spatially dependent factor  $\eta(\mathbf{r})$ . Such an increase can be understood by the diffraction effect due to which the longer wavelengths dominate the off-axis part of the pulses [11,12]. If the pulse width on axis is known, the pulse width at any point in space can be obtained from Eq. (2.16).

For the family of single-cycle pulses given by Eq. (2.15), the spatially resolved field amplitude spectrum is given by substituting Eq. (2.6) into Eq. (2.5) with  $\omega_0 = 0$ . The combination of the Gaussian beam size  $\exp[-\rho^2/w^2(z)]$  with  $\omega^p \exp(-\omega\tau_0)$  yields  $\omega^p \exp[-\omega\tau_0\eta(\mathbf{r})]$ , thus the peak frequency and wavelength of the single-cycle ( $\omega_0 = 0$ ) pulse at any spatial point are also related to those on axis by the scaling parameter through

$$\omega_p(\mathbf{r}) = \frac{\omega_p^o}{\eta(\mathbf{r})}; \quad \lambda_p(\mathbf{r}) = \lambda_p^o \eta(\mathbf{r}), \quad (2.18)$$

where

$$\omega_p^o = \frac{p}{\tau_0}, \quad \lambda_p^o = \frac{2\pi c \tau_0}{p} \quad (2.19)$$

are, respectively, the peak frequency and wavelength of the envelope spectrum on axis ( $\rho = 0, z$ ). For multicycle pulses described by Eq. (2.9), the peak frequency is given by

$$\omega_p(\mathbf{r}) = \omega_0 + \frac{\omega_p^o}{\eta(\mathbf{r})}. \quad (2.20)$$

Hence, the spatial variation of the frequency is independent of the pulse carrier. It is only determined by the spatial variation of the complex envelope frequency. The full width half-maximum (FWHM) bandwidth at any spatial point also satisfies the scaling law

$$\Delta\omega_{\text{FWHM}}(\mathbf{r}) = \frac{\Delta\omega_{\text{FWHM}}^o}{\eta(\mathbf{r})}, \quad (2.21)$$

where  $\Delta\omega_{\text{FWHM}}^o$  is the FWHM bandwidth on axis. Note that  $\eta(\mathbf{r}) = 1$  on axis. Thus, like the pulse width, the peak frequency and the FWHM bandwidth are invariant on axis due to the isodiffracting nature of the pulse. Off axis those values are scaled by the scaling parameter  $\eta(\mathbf{r})$ . As expected, the time-bandwidth product of these pulses is a constant everywhere in space. It is given by

$$\tau_p(\mathbf{r}) \Delta\omega_{\text{FWHM}}(\mathbf{r}) = \tau_p^o \Delta\omega_{\text{FWHM}}^o. \quad (2.22)$$

This value is only determined by the envelope spectrum, and not affected by propagation effects.

On the other hand, the pulses have a frequency chirp that is affected by diffraction. It varies spatially. From Eq. (2.9)

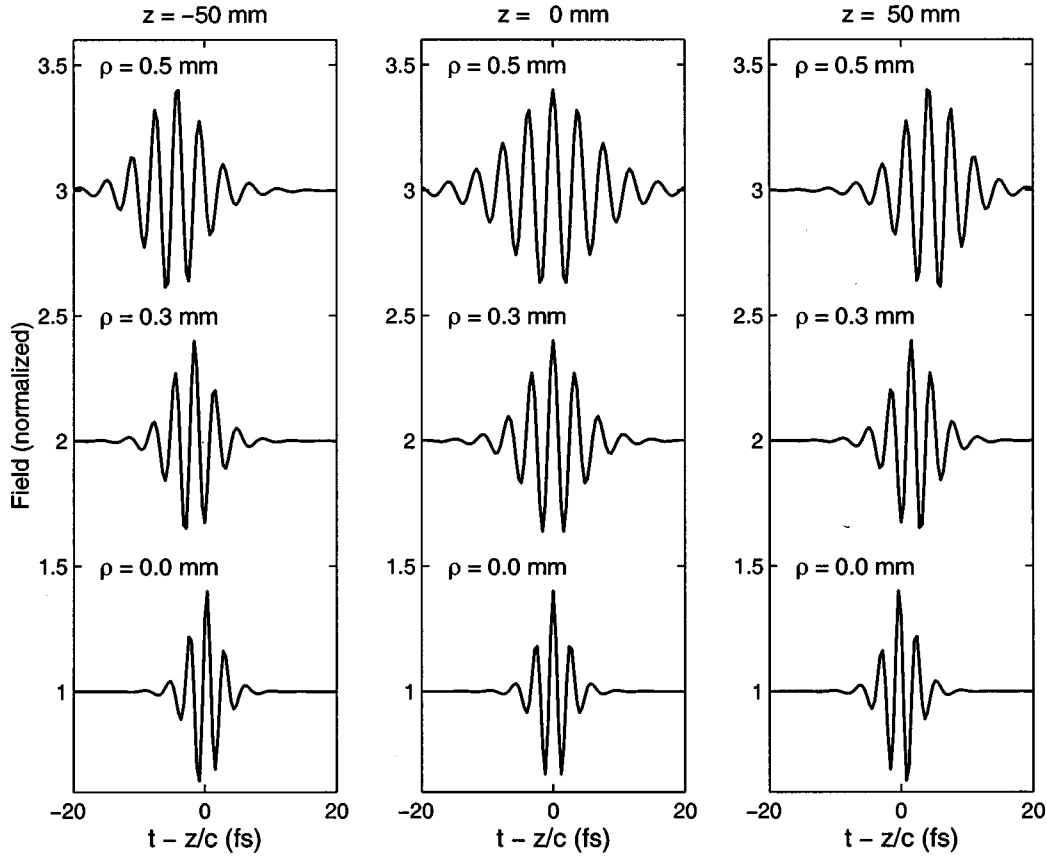


FIG. 3. Temporal waveforms of the pulse at different  $z$  and  $\rho$ . The pulse width, frequency, the number of cycles, and the absolute phase vary from point to point in space. The low-frequency cutoff  $f_0=0.2\text{ fs}^{-1}$  and  $\tau_0=5\text{ fs}$ . The beam waist, located at  $z=0$ , is  $w_0\approx 0.15\text{ mm}$ . Note the time delay  $\rho^2/2R(z)$  with respect to the pulse on axis in each column.

the instantaneous frequency can be defined by the derivative of the phase of the field with respect to time. It is the sum of the carrier frequency and the instantaneous frequency of the complex envelope function,

$$\omega_i(\mathbf{r}, T) = \frac{\partial}{\partial t} [\omega_0 \tau + \alpha(T)] = \omega_0 + \frac{\omega_a}{(1+T^2)\eta(\mathbf{r})}, \quad (2.23)$$

where  $\omega_a = (p+1)/\tau_0 = \omega_p^o(p+1)/p$ . Thus, the spatial variation of the instantaneous frequency and the chirping effect also come from the complex envelope. Equation (2.23) shows that the instantaneous frequency is symmetrically chirped about the pulse center ( $T=0$ ). The pulse center has a higher frequency than the leading and the trailing edges. It can be expected that these pulses will be steepened towards the trailing edge if they propagate in a medium with normal dispersion. Figure 4 shows the instantaneous frequency and the temporal waveforms of the pulse with carrier frequency  $f_0=0.2\text{ fs}^{-1}$  for points on axis ( $\eta=1$ ) and on the characteristic line  $\eta=2$ . The scaling nature of these pulses is clearly shown in the plots. The pulse width on the characteristic line  $\eta=2$  is twice that on axis ( $\eta=1$ ). After subtracting the low-frequency cutoff  $f_0=0.2\text{ fs}^{-1}$ , the instantaneous frequency on the characteristic line  $\eta=2$  is one half the value on axis.

Equations (2.16)–(2.23) show that these pulses obey a simple scaling law. All the temporal and frequency quantities are expressed in terms of the scaling parameter  $\eta(\mathbf{r})$  and the

corresponding axial values which are invariant upon propagation. The off-axis values scale as  $\eta(\mathbf{r})$ . The temporal and frequency quantities are the same for all spatial points that have the same value of  $\eta(\mathbf{r})$ , i.e., the characteristic lines  $\eta(\mathbf{r})=\text{const}$  [which are the hyperbolic rays  $\rho^2/a^2(z)=\text{const}$ ]. For this set of pulsed beams the temporal and frequency information travels along the characteristic lines. Thus, any physical quantities that depend on time and frequency are also invariant along the characteristic lines. The values of these quantities on different characteristic lines are simply related by the scaling parameter. To understand the scaling structure of these pulses, if one knows the information at an arbitrary point in space, one can easily predict the information in all of space by applying the scaling parameter. For single-cycle pulses ( $\omega_0=0$ ), if the pulse temporal profile on axis is known as  $E(z, t')$ , where  $t'=t-z/c$ , the temporal profile at any point in space can be obtained simply by shift and scaling, i.e.,

$$E(\mathbf{r}, t) = \frac{1}{\eta^{p+1}(\mathbf{r})} E \left\{ z, \frac{t' - \frac{\rho^2}{2R(z)c}}{\eta(\mathbf{r})} \right\}. \quad (2.24)$$

The scaling structure of these pulses is illustrated in Fig. 5, which shows the temporal waveforms along three characteristic lines. Along the characteristic lines the pulse is translationally invariant except for the absolute phase induced by the Gouy effect. On the different characteristic lines, the

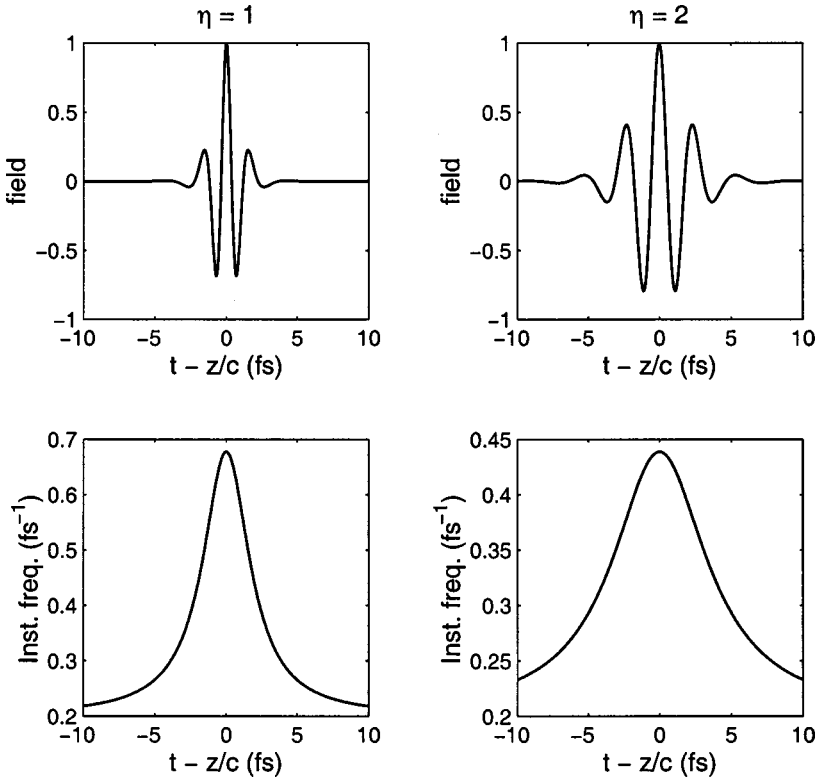


FIG. 4. Pulse temporal waveforms and the instantaneous frequencies on two different characteristic lines: on axis  $\eta(\mathbf{r})=1$  and  $\eta(\mathbf{r})=2$  for a low-frequency cutoff  $f_0=0.2 \text{ fs}^{-1}$  and  $\tau_0=2 \text{ fs}$ . The instantaneous frequencies are higher at the center  $T=0$  than those at the leading and trailing edges of the pulse. Note the scaling character of these pulses. The pulse width on  $\eta(\mathbf{r})=2$  is about twice that on axis. After subtracting the low-frequency cutoff  $f_0=0.2 \text{ fs}^{-1}$ , the instantaneous frequency on  $\eta(\mathbf{r})=2$  is one half that on axis.

pulse self-scales as the values of the corresponding lines. The local (radial) time delay  $\rho^2/2cR(z)$  along the characteristic lines is given by  $(\eta-1)\tau_0 z/z_R$ .

It is the same spatially dependent scaling parameter  $\eta(\mathbf{r})$  which lengthens the pulse width, narrows the bandwidth, and decreases the instantaneous frequencies towards the pulse periphery. Such a simple scaling structure of these eigen-

pulses is the result of isodiffraction and the spectra Eq. (2.6). The scaling structure is built in the complex envelope, which is affected by the focusing geometry and the envelope spectrum. Note if  $z_R \rightarrow \infty$ , then  $\eta(\mathbf{r}) \rightarrow 1$ , and  $R(z) \rightarrow \infty$ ; thus, there will be neither scaling nor curvature.

### B. Ripples

One of the results of the spatial variations of the instantaneous frequency and the bandwidth is the possibility of developing ripples at the leading and trailing edges of the pulses towards the pulse periphery. The consequence of this is that a single-cycle pulse may self-transform gradually into a multiple-cycle pulse along the radial direction. This situation can occur when the peak frequency and bandwidth of the spectrum change at different rates along the radial direction, and can be characterized by the ratio of the peak frequency to the bandwidth. This effect is shown in Fig. 6 for two different spectra at two values of the scaling parameter. Figure 6(a) represents a single-cycle pulse ( $f_0=0$ ), while Fig. 6(b) is for a pulse with the low-frequency cutoff  $f_0=0.1 \text{ fs}^{-1}$ . The temporal waveforms of these two pulses, while similar on axis [ $\eta(\mathbf{r})=1$ ], are quite different off axis [ $\eta(\mathbf{r})>1$ ]. One pulse maintains its single-cycle character in the whole space, while the other develops ripples towards the pulse periphery.

The ratio of the peak frequency to the bandwidth ( $\gamma$ ) is of course equal to the ratio of the pulse length to the period of the carrier. This ratio therefore characterizes the approximate number of cycles in the pulse. In general, the ratio of the peak frequency to the bandwidth is a function of spatial variables since the peak frequency and bandwidth change spatially. When the value of  $\gamma$  is less than 1, the pulse reveals a single-cycle character. When the value of  $\gamma$  exceeds 1, the original single-cycle pulse will develop new cycles of small

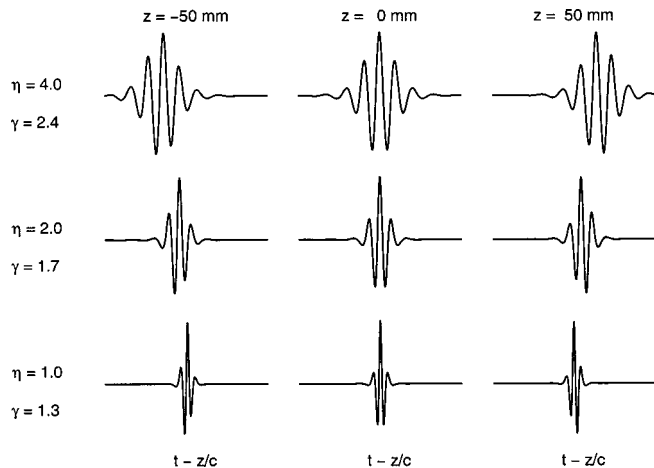


FIG. 5. Temporal waveforms of the pulse along three characteristic lines. The pulse width, frequency, and the number of cycles are invariant along the same lines. The waveforms on different characteristic lines are related by the scaling parameter  $\eta(\mathbf{r})$ . The phase differences on the same line come from the Gouy phase shift, which represents the absolute phase of the pulses. All the fields are normalized by their peak values. Note the time reversal property on passing through the waist  $z=0$ . The time delay increases as  $\eta(\mathbf{r})$  increases due to the curvature of the converging and diverging phase fronts.  $\gamma$  is the ratio of the peak frequency to the bandwidth.  $f_0=0.1 \text{ fs}^{-1}$  and  $\tau_0=3 \text{ fs}$ .

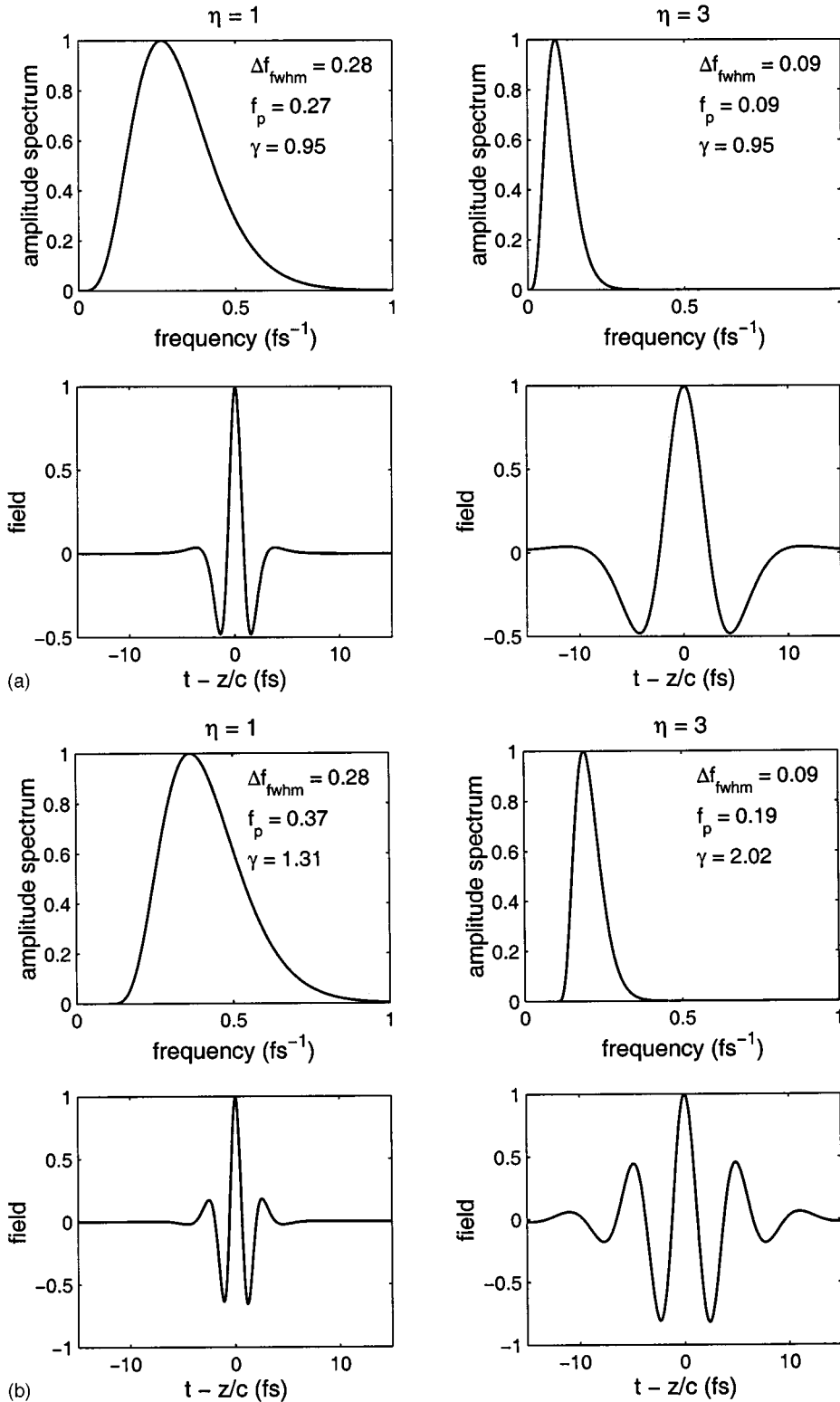


FIG. 6. (a) Temporal waveforms and spectra on and off axis. The low-frequency cutoff  $f_0=0$  and  $\tau_0=3$  fs. Even though the peak frequency and the bandwidth vary in the space, their ratio is invariant when  $f_0=0$ . Thus, the pulse maintains its single-cycle character everywhere in the space. (b) Temporal waveforms and spectra on and off axis. The low-frequency cutoff  $f_0=0.1$  fs $^{-1}$  and  $\tau_0=3$  fs. The temporal waveform on axis ( $\eta=1$ ) is similar to that in (a); however, the off axis waveforms are different due to the different low-frequency cutoff. The pulse develops more ripples towards the pulse periphery. The peak frequency and bandwidth, as well as their ratio, vary in the space. The value of  $\gamma$ , and hence the number of cycles increase as one moves away from the axis.

amplitude at the leading and trailing edges of the pulse. The higher the value of  $\gamma$ , the more cycles the pulse has. The value of  $\gamma$  characterizes the number of cycles and the transition from single to multiple cycles. In Figs. 6(a) and 6(b), even though the spectral shapes and bandwidths are exactly the same everywhere in space, their peak frequencies are different because of the different values of the low-frequency cutoff  $\omega_0$ . This leads to different values of  $\gamma$  for the two cases. The spatial variation of the ratio of the peak frequency

to the bandwidth can be obtained from Eqs. (2.20) and (2.21), and is given by

$$\gamma(\mathbf{r}) = \frac{\omega_p^o + \omega_0 \eta(\mathbf{r})}{\Delta \omega_{\text{FWHM}}^o}. \quad (2.25)$$

The values of  $\gamma$  are listed in Fig. 6. When the low-frequency cutoff  $\omega_0=0$ ,  $\gamma$  is invariant in space even though the peak frequency and bandwidth change spatially. This explains

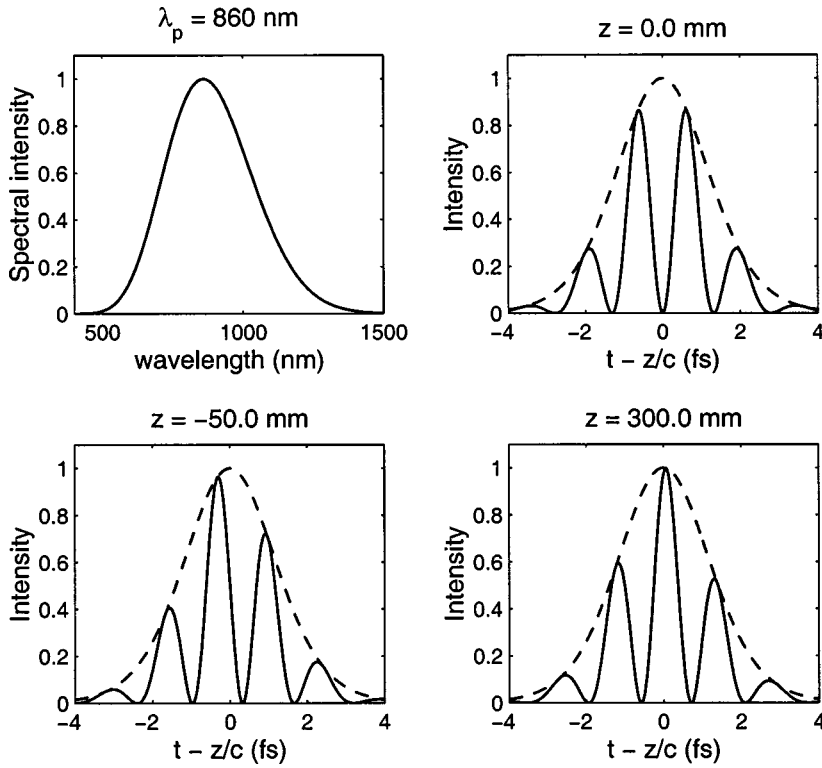


FIG. 7. Gouy phase shift is the source of the absolute phase of the ultrashort pulses propagating in a dispersionless medium. The left upper plot is the spectral intensity of a two-cycle pulse. The other three plots show how the carrier wave of this pulse slides underneath the envelope on passing through the waist ( $z=0$ ), as a result of the phase and envelope velocity mismatch due to the Gouy phase shift. The dashed lines represent the time-averaged intensity, while the solid lines are the underlying oscillations. In the plot  $f_0 = 0.15 \text{ fs}^{-1}$  and  $\tau_0 = 4 \text{ fs}$ .

why the pulse with  $\omega_0=0$  [Fig. 6(a)] maintains its single-cycle character everywhere in space. On the other hand, when the low-frequency cutoff  $\omega_0 \neq 0$ , the ratio of the peak frequency to the bandwidth will vary in space. Thus, the pulse will develop ripples off axis, as shown in Fig. 6(b). The number of cycles is conserved along the characteristic lines [ $\eta(\mathbf{r}) = \text{const}$ ].

### C. Absolute phase

The phase of these pulses in the time domain is given by the complex exponential part [ $\exp(i\psi)$ ] of Eq. (2.9). That is,

$$\psi(\mathbf{r}, t) = -\omega_0 \tau - \alpha_p(T) - \phi(z), \quad (2.26)$$

where the definitions of  $T$  and  $\tau$  are given by Eqs. (2.11) and (2.12), respectively. The first term  $\omega_0 \tau$  represents the fast (if  $\omega_0 \gg \Delta\omega_{\text{FWHM}}$ ) oscillation due to the carrier. The second term  $\alpha_p(T)$  represents the slow modulation due to the finite bandwidth. The Gouy phase shift  $\phi(z)$  is the only term that is independent of the spectrum. It is the Gouy phase shift that causes the carrier to slide underneath the envelope during propagation. This is shown in Fig. 7, which plots the spectrum of the pulse, the pulse intensity envelope  $|A_p|^2$  (equal to the time-averaged intensity), and the underlying oscillation of a femtosecond pulse at three propagation distances. The difference between the phase and envelope velocities is due to the Gouy effect. This absolute phase due to the Gouy shift has implications for recirculating pulses in a curved mirror resonator such as a mode-locked laser cavity. Even in the absence of intracavity dispersive or nonlinear elements the accumulated Gouy phase shift causes the absolute phase to be different for successive pulses. This results in a pulse shape instability in which the output temporal profile varies from pulse to pulse. For example, consider a symmetric resonator with mirrors of radius of curvature  $R$  spaced by a dis-

tance  $L$ . The cavity forces all the frequency components of the pulse to have the same Rayleigh range given by [9]

$$z_R = \frac{\sqrt{L(2R-L)}}{2}. \quad (2.27)$$

Since the waist of the pulsed beam is located at the cavity center ( $z=0$ ), in one round trip the Gouy shift is

$$\phi_{\text{RT}} = 4 \tan^{-1} \sqrt{\frac{L}{2R-L}}. \quad (2.28)$$

After the  $n$ th round trip the accumulated Gouy shift is  $n\phi_{\text{RT}}$ . Figure 8 shows the pulse profiles for the intensity envelope and the underlying oscillation of successive two-cycle pulses in a cavity with  $R=200 \text{ mm}$  and  $L=182 \text{ mm}$ . The absolute phase, and hence the temporal profile, are different after each round trip inside the cavity.

### D. Gouy shift, Hilbert transform, and time derivative

As shown quite generally by Heyman [6] and confirmed by us for our specific isodiffracting pulses [5], these eigen-wave packets undergo a Hilbert transform along hyperbolic trajectories as they propagate from the beam waist to the far field. For two points ( $z=0, \rho_1$ ) and ( $z=z_2, \rho_2$ ) that do not necessarily lie on the same hyperbolic trajectory (i.e., different pulse widths), the temporal waveforms are related by a scaled Hilbert transform which, for the single-cycle pulse of Eq. (2.15), is given by

$$\text{Re}\{E_p^+(z_2, \rho_2, \tau_2)\} = \frac{S^{p+1}}{d\pi} \text{P} \int_{-\infty}^{+\infty} \frac{\text{Re}\{E_p^+(0, \rho_1, t')\}}{S\tau_2 - t'} dt', \quad (2.29)$$

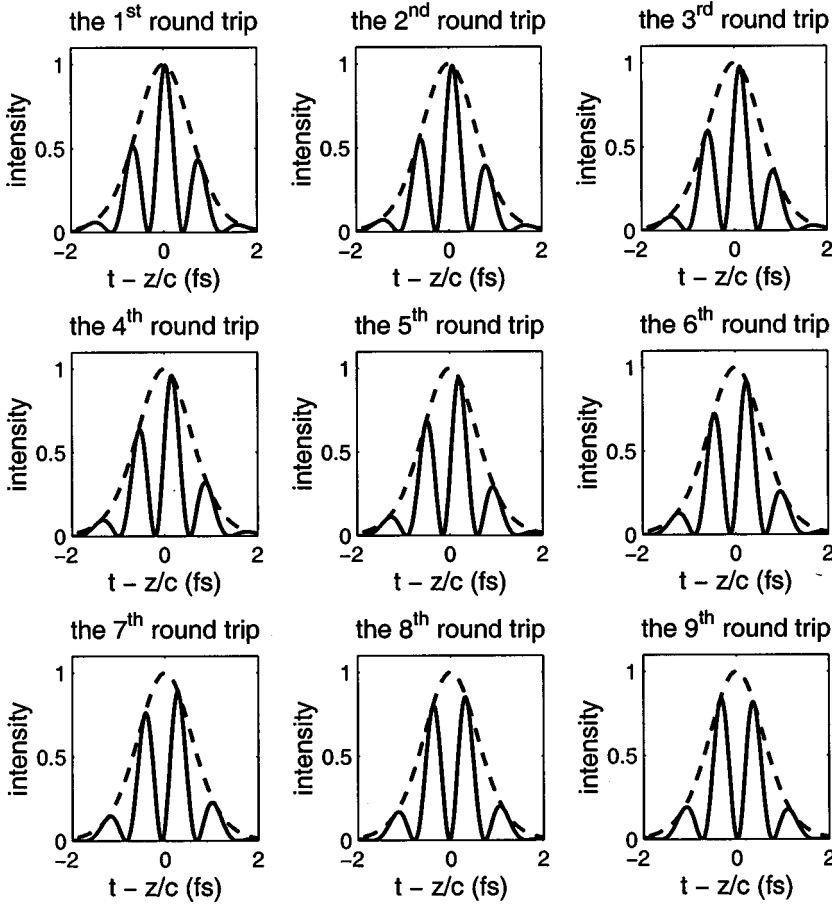


FIG. 8. Profiles of the intensity envelope (a time-averaged intensity) and the underlying oscillation of a recirculating two-cycle pulse inside a symmetric laser cavity (radii of mirrors  $R = 200$  mm and separation  $L = 182$  mm). The absolute phase and temporal waveform are different from pulse to pulse. The dashed lines represent the intensity envelope, while the solid lines are the underlying oscillations. Here,  $f_0 = 0.2$  fs $^{-1}$  and  $\tau_0 = 2$  fs.

$$\text{Im}\{E_p^+(z_2, \rho_2, \tau_2)\} = -\frac{S^{p+1}}{d\pi} P \int_{-\infty}^{+\infty} \frac{\text{Im}\{E_p^+(0, \rho_1, t')\}}{S\tau_2 - t'} dt',$$

where

$$\tau_2 = t - \frac{1}{c} \left\{ z_2 + \frac{\rho_2^2}{2R(z_2)} \right\}. \quad (2.30)$$

Here the relative scaling parameter  $S = \eta(0, \rho_1) / \eta(z_2, \rho_2)$  depends on the coordinates of these two points.  $d = \sqrt{1 + (z_2/z_R)^2}$ , and  $P$  stands for the principal value of the integral. For points on the same hyperbolic trajectory,  $S = 1$ , and thus Eq. (2.29) reduces to the Hilbert transform.

For any initial field spectrum  $\tilde{U}_0(x_0, y_0, \omega)$  the field at any plane  $z$  in the paraxial approximation is given by the Kirchhoff diffraction integral

$$\begin{aligned} \tilde{U}(x, y, z, \omega) &= \frac{-i\omega}{2\pi cz} \iint_s \tilde{U}_0(x_0, y_0, \omega) \\ &\times \exp \left\{ ikz + ik \frac{(x-x_0)^2 + (y-y_0)^2}{2z} \right\} dS, \end{aligned} \quad (2.31)$$

where  $k = \omega/c$  and the factor  $-i\omega$  implies a time derivative of the result of the above spatial integration. In particular, suppose the initial field is the isodiffracting solution of Eq. (2.5) evaluated at  $z=0$ ,

$$\tilde{U}_0(x_0, y_0, \omega) = \frac{i}{z_R} \exp \left\{ -\frac{k(x_0^2 + y_0^2)}{2z_R} \right\} \tilde{F}(\omega). \quad (2.32)$$

Since  $k = \omega/c$  this initial field is not separable into a function of  $\omega$  and a function of  $(x_0, y_0)$ . Upon substituting this field in the Kirchhoff integral, the axial field is found to be

$$\tilde{U}(0, 0, z, \omega) = \frac{\tilde{F}(\omega) \exp(ikz)}{z - iz_R}, \quad (2.33)$$

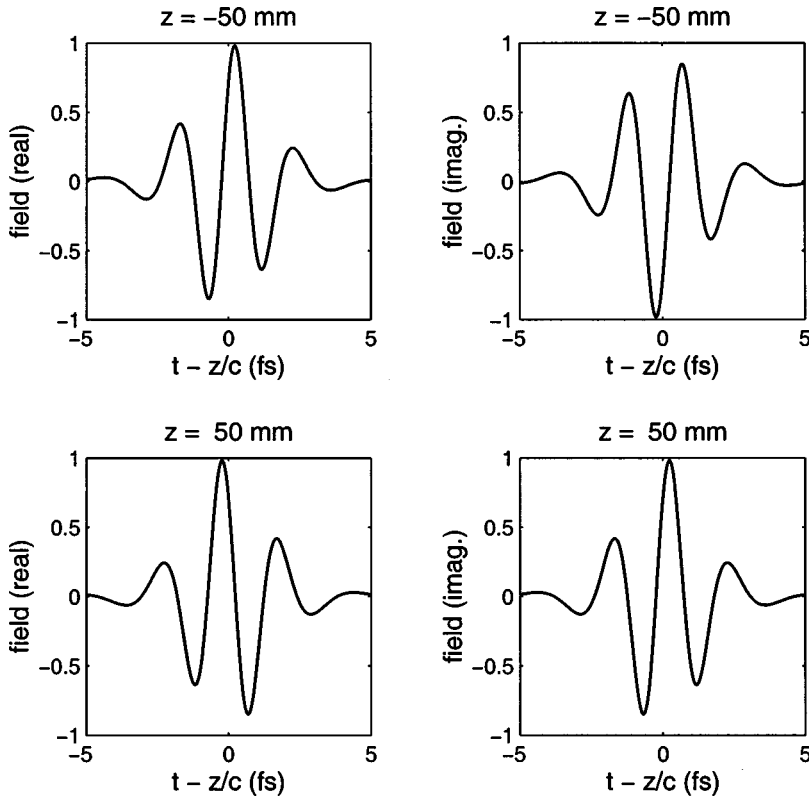
where the phase of the factor  $(z - iz_R)^{-1}$  is the Gouy shift. The spatial integration introduced a factor  $\omega^{-1}$  which cancels the time derivative operator in Eq. (2.31). In the far zone ( $z \rightarrow \infty$ ) the relation between the diffracted field and the initial field is

$$\begin{aligned} \tilde{U}(0, 0, z \rightarrow \infty, \omega) &\approx -i \frac{z_R}{z} \tilde{U}(0, 0, z=0, \omega) \exp(ikz), \\ &\text{for } \omega > 0. \end{aligned} \quad (2.34)$$

The factor of  $-i$  in the above expression gives rise to the Hilbert transform relationship between far field and near field temporal profiles.

Since the pulse solution Eq. (2.9) is an analytic signal, its real and imaginary parts at any point  $\mathbf{r}$  are temporal Hilbert transforms of each other. In addition they obey certain space-time symmetries also noted by Kaplan [11],

$$\text{Im}\{E_p^+(-z, \rho, -t)\} = -\text{Im}\{E_p^+(z, \rho, t)\}, \quad (2.35)$$



$$\text{Re}\{E_p^+(-z, \rho, -t)\} = \text{Re}\{E_p^+(z, \rho, t)\}.$$

The imaginary part is antisymmetric, while the real part is symmetric under simultaneous reversal of  $t$  and  $z$ . In passing through the beam waist the antisymmetric pulse at  $z=0$  experiences both time and polarity reversals, while the symmetric pulse only experiences a time reversal. These properties can be seen from Fig. 9.

The critical condition to observe the time reversal is that the pulse shape at the beam waist should be either symmetric or antisymmetric, i.e., the initial phase (absolute phase) at the beam waist is either zero or  $\pi/2$ . Since the focal plane is a symmetry plane of the propagation, the symmetry property requires that the same event should occur whether the pulse propagates from the focal plane to the right or to the left. In Fig. 10(a), if the right-hand side of the pulse becomes more negative while propagating from the focal plane to point B, the symmetric pulse shape on the focal plane implies that the left-hand side of the pulse should become more negative in propagating from the focal plane to point A. Since propagation to the left and to the right are time-reversed versions of each other, the fields at point A and point B are time reversed. Similarly, in Fig. 10(b), if the field at point B has a positive polarity with a lower left lobe, the antisymmetric pulse shape on the focal plane implies that the field at point A should have a negative polarity with a higher right lobe for a logically self-consistent result. In this case both time and polarity reversals can be seen from Fig. 10(b).

### E. Diffraction and pulse energy

For ultrashort pulses the beam size generally depends on both the carrier frequency and the pulse bandwidth [4]. This

FIG. 9. Temporal waveforms of two-cycle pulses of real (left) and imaginary (right) solutions at equal distances on both sides of the waist. The imaginary solution, which is antisymmetric at the waist, experiences both time and polarity reversals in passing through the waist. However, only a time reversal can be seen in the real solution, which is symmetric at the waist. Both time and polarity reversals are the effects of a phase shift. The carrier frequency  $f_0 = 0.2 \text{ fs}^{-1}$  and  $\tau_0 = 3 \text{ fs}$ .

can be seen from the transverse dependence of the magnitude of the wave packet solution in Eq. (2.9),

$$\left[1 + \frac{\rho^2}{a^2(z)}\right]^{-(p+1)} \exp[-\rho^2/w^2(z)]. \quad (2.36)$$

The two factors above determine the contributions of the pulse bandwidth and carrier frequency to the spot size. At the waist of the pulsed beam ( $z=0$ ) the pulse bandwidth ( $1/\tau_0$ ) characterizes the transverse extent of the envelope,  $a_0^2$

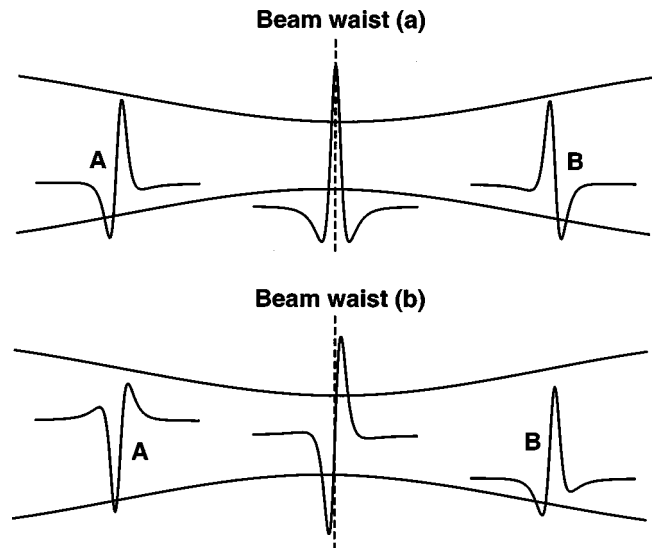


FIG. 10. Spatial symmetry of the Gaussian beam geometry explains the time and the polarity reversals when an isodiffracting pulse passes through the waist. The focal plane is a symmetry plane of the isodiffracting PGB.

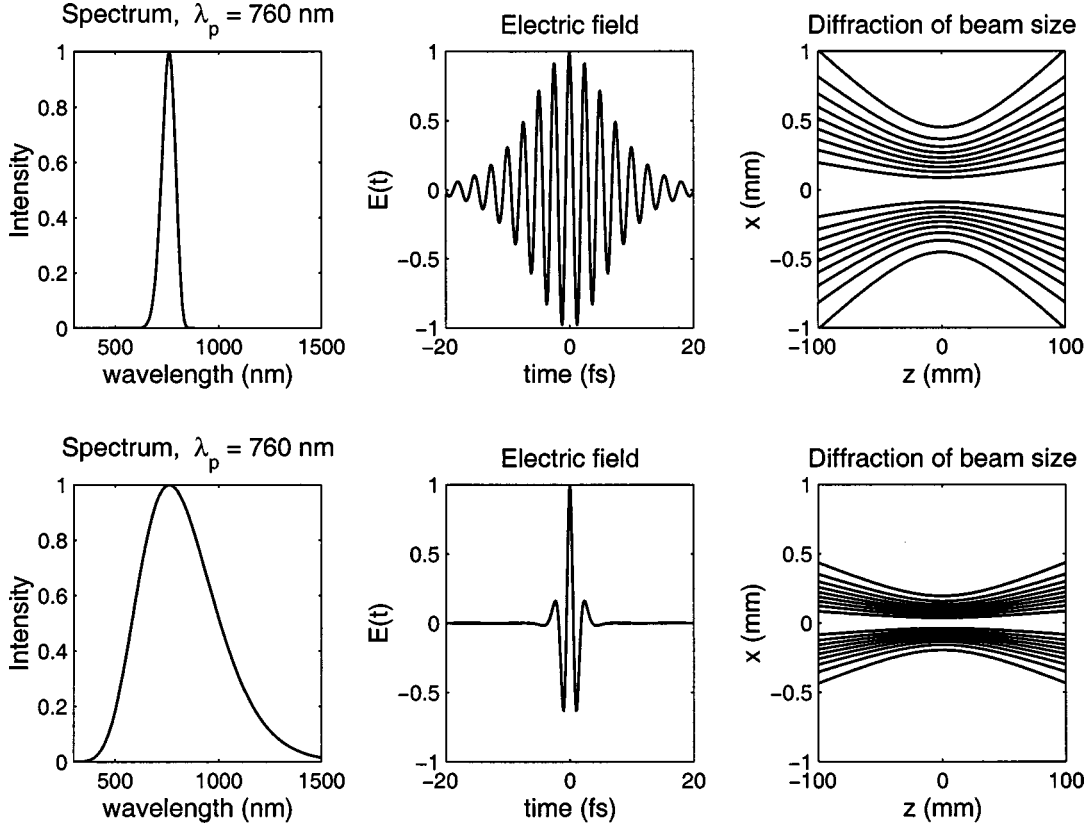


FIG. 11. Effect of the bandwidth spatial confinement. The left two plots are the spectral intensity of two pulses with the same peak frequency, but different bandwidths.  $f_0 = 0.34 \text{ fs}^{-1}$  and  $\tau_0 = 14.5 \text{ fs}$  for the top spectrum, while  $f_0 = 0.1 \text{ fs}^{-1}$  and  $\tau_0 = 2.7 \text{ fs}$  for the bottom one. The middle two plots are the corresponding electric fields. The right two plots show the evolutions of the beam size of the corresponding two pulses. The beam sizes in the plot are defined by one-tenth of the values on axis. The beam sizes of the two ultrashort pulses with the same peak wavelength, but the different bandwidths are significantly different. Keeping the peak frequency unchanged, the transverse dimension of the pulse can be reduced by increasing the bandwidth to the order of the peak frequency.

$= 2c\tau_0 z_R$ . The carrier frequency in turn characterizes the transverse dimension of the carrier,  $w_0^2 = 2cz_R/\omega_0$ . For a single-cycle pulse ( $\omega_0 = 0$ ), only the first factor in Eq. (2.36) contributes to the beam size, which decreases with increasing bandwidth as higher frequencies begin to dominate the spectrum. At the other extreme, for quasimonochromatic pulses ( $\omega_0 \gg 1/\tau_0$ ), only the exponential factor makes a significant contribution to the beam size  $w^2(z)$ , which evolves in the same manner as a monochromatic Gaussian beam. Moreover, Eq. (2.36) implies one can confine the transverse extent of ultrashort pulses along the propagation axis by increasing the bandwidth (keeping the peak frequency unchanged) up to the order of the peak frequency. This effect of the bandwidth spatial confinement is shown in Fig. 11 in which two pulses have the same peak frequency, but different bandwidths. The beam sizes are significantly different.

The pulse intensity and pulse energy diffract differently for ultrashort pulses [13,14]. The diffraction of the entire pulse is easy to characterize by diffraction of the pulse energy. Using the method described in Ref. [5] the diffraction of the pulse energy of the family of single-cycle pulses given by Eq. (2.15) is characterized by

$$\Gamma(\mathbf{r}) \propto \frac{1}{(z^2 + z_R^2)} \frac{1}{\left\{1 + \frac{\rho^2}{a^2(z)}\right\}^{2p+1}} = \frac{1}{(z^2 + z_R^2)} \frac{1}{\eta^{2p+1}(\mathbf{r})}. \quad (2.37)$$

Equation (2.37) describes the energy density on transverse planes at different propagation distances. It shows that the energy is invariant along characteristic lines. Its space trajectory depicts the diffraction of the pulse energy. Thus, Eq. (2.37) can be used to find the radial extent of the pulse energy on any transverse plane. We use the Gaussian criterion to characterize the width of the energy distribution of the pulse,

$$\frac{\Gamma(z, \rho)}{\Gamma(z, 0)} = \frac{1}{\left\{1 + \frac{\rho^2}{a^2(z)}\right\}^{2p+1}} = \left(\frac{1}{e}\right)^2. \quad (2.38)$$

Using the approximation  $\exp[2/(2p+1)] - 1 \approx 1/p$  (when  $p = 1$  the error is 5%, and when  $p = 2$  the error is only 1%), one finds that the diffraction of the pulse energy resembles that of a monochromatic Gaussian beam of effective wavelength equal the peak wavelength of the envelope spectrum. The radius of the energy distribution evolves as

$$w_e^2(z) = w_e^2 \left\{1 + \left(\frac{z}{z_R}\right)^2\right\} = \frac{a^2(z)}{p}, \quad (2.39)$$

where  $a^2(z)$  is given by Eq. (2.14), and

$$w_e^2 = \frac{\lambda_p^2 z_R}{\pi}. \quad (2.40)$$

A useful result for isodiffracting single-cycle pulses is that the width of the energy distribution and the pulse width are related. This is not true for multiple-cycle pulses whose beam size is determined by the diffraction of both carrier and envelope. Eliminating  $\lambda_p^o$  from Eqs. (2.17) and (2.40), one obtains

$$\tau_p^o = \sqrt{2p} \frac{w_e^2}{cz_R}. \quad (2.41)$$

Therefore, by measuring the beam waist of the distribution of the pulse energy and the Rayleigh range, one can easily obtain the on-axis pulse width of isodiffracting single-cycle pulses with the use of Eq. (2.41).

### III. CONCLUSIONS

In summary, we have presented an analysis of the spatiotemporal evolution of ultrashort pulses within the paraxial beam approximation. For the set of spectra given in Sec. II, certain simple scaling laws permit a deep qualitative under-

standing of the spatial variations of the pulse width, bandwidth, and instantaneous frequency. For pulses evolving in a cavity, we find that the absolute phase of the circulating pulses varies in each round trip due to the Gouy phase shift, which is determined by the cavity geometry. We have also shown that the ability of a pulse to retain its single-cycle character in the whole space depends on the spatial variation of the spectrum. The pulse spectrum (peak frequency and bandwidth) and its spatial variation set a limit on the number of cycles of an ultrashort pulse generated in experiments. The analysis is applicable to isodiffracting pulsed Gaussian beams such as those produced by a mode-locked laser. Our results may be useful in ultrashort pulse communications, as well as in the characterization and understanding of terahertz pulses and femtosecond optical pulses.

### ACKNOWLEDGMENT

This work was partially supported by the National Science Foundation through the Center for Ultrafast Optical Science under Grant No. STC PHY 8920108.

- 
- [1] U. Morgner, F. Kärtner, S. Cho, Y. Chen, H. Haus, J. Fujimoto, E. Ippen, V. Scheuer, G. Angelow, and T. Tschudi, *Opt. Lett.* **24**, 411 (1999).
  - [2] For a collection of articles on terahertz generation, see *Terahertz Electromagnetic Pulse Generation, Physics, and Applications*, special issue of *J. Opt. Soc. Am. B* **11**, 2454 (1994).
  - [3] E. Heyman and T. Melamed, *IEEE Trans. Antennas Propag.* **AP-42**, 518 (1994).
  - [4] Z. Wang, Z. Zhang, Z. Xu, and Q. Lin, *IEEE J. Quantum Electron.* **33**, 566 (1997).
  - [5] S. Feng, H. G. Winful, and R. W. Hellwarth, *Phys. Rev. E* **59**, 4630 (1999).
  - [6] E. Heyman, *IEEE Trans. Antennas Propag.* **AP-42**, 311 (1994).
  - [7] R. W. Ziolkowski, *Phys. Rev. A* **39**, 2005 (1989).
  - [8] M. A. Porras, *Phys. Rev. E* **58**, 1086 (1998).
  - [9] A. E. Siegman, *Lasers* (University Science Books, Sausalito, 1986).
  - [10] S. Feng, H. G. Winful, and R. W. Hellwarth, *Opt. Lett.* **23**, 385 (1998); **23**, 1141 (1998).
  - [11] A. E. Kaplan, *J. Opt. Soc. Am. B* **15**, 951 (1998).
  - [12] D. You and P. H. Bucksbaum, *J. Opt. Soc. Am. B* **14**, 1651 (1997).
  - [13] R. W. Ziolkowski and J. B. Judkins, *J. Opt. Soc. Am. A* **9**, 2021 (1992).
  - [14] G. C. Sherman, *J. Opt. Soc. Am. A* **6**, 1382 (1989).